Realtime photoacoustic microscopy *in vivo* with a 30-MHz ultrasound array transducer

Roger J. Zemp,[1,3] Liang Song,[1] Rachel Bitton,[2] K. Kirk Shung,[2] and Lihong V. Wang[1,*]

[1]Washington University, Optical Imaging Laboratory, Department of Biomedical Engineering, Saint Louis, Missouri 63130
[2]University of Southern California, Department of Biomedical Engineering, Los Angeles, California 90089
[3]Current address: Department of Electrical and Computer Engineering, University of Alberta, 9107-116 St. Edmonton, Alberta, Canada, T6G 2V4, zemp@ece.ualberta.ca
*Corresponding author: lhwang@biomed.wustl.edu

Abstract: We present a novel high-frequency photoacoustic microscopy system capable of imaging the microvasculature of living subjects in realtime to depths of a few mm. The system consists of a high-repetition-rate Q-switched pump laser, a tunable dye laser, a 30-MHz linear ultrasound array transducer, a multichannel high-frequency data acquisition system, and a shared-RAM multi-core-processor computer. Data acquisition, beamforming, scan conversion, and display are implemented in realtime at 50 frames per second. Clearly resolvable images of 6-μm-diameter carbon fibers are experimentally demonstrated at 80 μm separation distances. Realtime imaging performance is demonstrated on phantoms and *in vivo* with absorbing structures identified to depths of 2.5-3 mm. This work represents the first high-frequency realtime photoacoustic imaging system to our knowledge.

© 2008 Optical Society of America

OCIS codes: (110.5120) Photoacoutic imaging; (110.5100) Phased-array imaging systems; (110.7170) Ultrasound; (170.3880) Medical and biological imaging; (170.3890) Medical optics instrumentation.

References and links

1. T. F. Massoud, and S. S. Gambhir, "Molecular imaging in living subjects: seeing fundamental biological processes in a new light," Genes Dev. **17**, 545-580 (2003).
2. C. Abbey, A. Borowsky, J. Gregg, E. McGoldrick, R. Cardiff, and S. Cherry, "Longitudinal correlations in a small-animal PET studies," Med. Phys. **32**, 1901-1901 (2005).
3. P. A. Dayton, and K. W. Ferrara, "Targeted imaging using ultrasound," J. Magn. Res. **16**, 362-377 (2002).
4. O. Couture, P. D. Bevan, E. Cherin, K. Cheung, P. N. Burns, and F. S. Foster, "Investigating perfluorohexane particles with high-frequency ultrasound," Ultrasound. Med. Biol. **32**, 73-82 (2006).
5. M. H. Xu, and L. H. V. Wang, "Photoacoustic imaging in biomedicine," Rev. Sci. Instrum. **77**, - (2006).
6. A. Dunn, and D. Boas, "Transport-based image reconstruction in turbid media with small source-detector separations," Opt. Lett. **25**, 1777-1779 (2000).
7. E. M. C. Hillman, D. A. Boas, A. M. Dale, and A. K. Dunn, "Laminar optical tomography: demonstration of millimeter-scale depth-resolved imaging in turbid media," Opt. Lett. **29**, 1650-1652 (2004).
8. G. Ku, X. D. Wang, X. Y. Xie, G. Stoica, and L. H. V. Wang, "Imaging of tumor angiogenesis in rat brains in vivo by photoacoustic tomography," Appl. Opt. **44**, 770-775 (2005).
9. X. D. Wang, Y. J. Pang, G. Ku, X. Y. Xie, G. Stoica, and L. H. V. Wang, "Noninvasive laser-induced photoacoustic tomography for structural and functional in vivo imaging of the brain," Nat. Biotechnol. **21**, 803-806 (2003).
10. K. Maslov, G. Stoica, and L. V. H. Wang, "In vivo dark-field reflection-mode photoacoustic microscopy," Opt. Lett. **30**, 625-627 (2005).
11. H. F. Zhang, K. Maslov, G. Stoica, and L. H. V. Wang, "Functional photoacoustic microscopy for high-resolution and noninvasive in vivo imaging," Nat. Biotechnol. **24**, 848-851 (2006).
12. M. Sivaramakrishnan, K. Maslov, H. F. Zhang, G. Stoica, and L. V. Wang, "Limitations of quantitative photoacoustic measurements of blood oxygenation in small vessels," Phys. Med. Biol **52**, 1349-1361 (2007).
13. X. D. Wang, X. Y. Xie, G. N. Ku, and L. H. V. Wang, "Noninvasive imaging of hemoglobin concentration and oxygenation in the rat brain using high-resolution photoacoustic tomography," J. Biomed. Opt. **11**, 024015 (2006).

14. L. Li, R. J. Zemp, G. Lungu, G. Stoica, and L. V. Wang, "Photoacoustic imaging of lacZ gene expression in vivo," J. Biomed. Opt. **12**, 020504 (2007).
15. M. Li, J. Oh, X. X., G. Ku, W. Wang, C. Li, G. Lungu, G. Stoica, and L. V. Wang, "Simultaneous molecular and hypoxia imaging of brain tumors in vivo using spectroscopic photoacoustic tomography," Proc. IEEE (Accepted 2007).
16. J. J. Niederhauser, M. Jaeger, R. Lemor, P. Weber, and M. Frenz, "Combined ultrasound and optoacoustic system for real-time high-contrast vascular imaging in vivo," IEEE Trans. Med. Imag. **24**, 436-440 (2005).
17. R. O. Esenaliev, A. A. Karabutov, and A. A. Oraevsky, "Sensitivity of laser opto-acoustic imaging in detection of small deeply embedded tumors," IEEE J. Select. Top. Quantum Electron. **5**, 981-988 (1999).
18. A. A. Oraevsky, S. L. Jacques, and F. K. Tittel, "Measurement of tissue optical properties by time-resolved detection of laser-induced transient stress," Appl. Opt. **36**, 402-415 (1997).
19. R. A. Kruger, W. L. Kiser, D. R. Reinecke, and G. A. Kruger, "Thermoacoustic computed tomography using a conventional linear transducer array," Med. Phys. **30**, 856-860 (2003).
20. R. Kruger, W. Kiser, D. Reinecke, and G. Kruger, "Molecular imaging with thermoacoustic computed tomography," Med. Phys. **30**, 1542-1542 (2003).
21. E. Zhang, and P. Beard, "Broadband ultrasound field mapping system using a wavelength tuned, optically scanned focused laser beam to address a Fabry Perot polymer film sensor," IEEE Trans. Ultrason. Ferroelectr. Freq. Control **53**, 1330-1338 (2006).
22. R. J. Zemp, R. Bitton, M. L. Li, K. K. Shung, G. Stoica, and L. V. Wang, "Photoacoustic imaging of the microvasculature with a high-frequency ultrasound array transducer," J. Biomed. Opt. **12**, 010501 (2007).
23. J. M. Cannata, J. A. Williams, Q. F. Zhou, T. A. Ritter, and K. K. Shung, "Development of a 35-MHz piezo-composite ultrasound array for medical imaging," IEEE Trans. Ultrason. Ferroelectr. Freq. Control **53**, 224-236 (2006).
24. R. Bitton, R. Zemp, L. Meng-Lin, J. Yen, L. H. Wang, and K. K. Shung, "Photoacoustic Microscopy with a 30 MHz Array and Receive System," in *IEEE Ultrasonics Symposium* (IEEE, 2006), pp. 389-392.
25. K. Wall, and G. R. Lockwood, "Modern implementation of a realtime 3D beamformer and scan converter system," in *Ultrasonics Symposium* (2005), pp. 1400-1403.
26. C.H. Hu, X.C. Xu, J.M. Cannata, J.T. Yen, K.K. Shung, "Development of a real-time, high-frequency ultrasound digital beamformer for high-frequency linear array transducers," IEEE Trans. Ultrason. Ferroelectr. Freq. Control, **53**, 317-323 (2006).
27. G. E. Moore, "Cramming More Components Onto Integrated Circuits," Proc. IEEE **86**, 82-85 (1998).
28. S. A. Telenkov, B. S. Tanenbaum, D. M. Goodman, J. S. Nelson, and T. E. Milner, "In vivo infrared tomographic imaging of laser-heated blood vessels," IEEE Journal of Selected Topics in Quantum Electronics **5**, 1193-1199 (1999).
29. J. S. Nelson, T. E. Milner, B. S. Tanenbaum, D. M. Goodman, and M. J. C. VanGemert, "Infra-red tomography of port-wine-stain blood vessels in human skin," Lasers in Medical Science **11**, 199-204 (1996).
30. D. Napolitano, C. Ching-Hua, G. W. McLaughlin, D. DeBusschere, L. Y. L. Mo, and J. Ting-Lan, "Zone-based B-mode imaging," in *IEEE Ultrasonics Symposium,* (IEEE, 2003), pp. 25-28.

1. Introduction

Traditional diagnostic imaging methods offer clinicians the ability to non-invasively visualize anatomy and judge pathology based on tissue morphology. While anatomical visualization has served the biomedical community well, there has been much recent progress in imaging methods providing molecular and functional information [1]. The surge of biomedical research spawned by the completion of the human genome project is opening new windows of opportunity for bio-imaging in medicine to elucidate genotype-phenotype relationships. Since mice possess surprising genetic homology with humans, they have emerged as an important means of studying disease, and many imaging techniques have evolved specifically for imaging small animals. Such small animal imaging modalities are accelerating biomedical research and enabling longitudinal studies in the same animal over time, rather than necessitating a population of animals sacrificed at various time points, thus avoiding the statistical plague of inter-subject variability [2].

In the clinic, time is critical and there is an increasing demand for realtime imaging techniques for immediate operator-feedback. Because modern ultrasound systems offer realtime imaging capabilities, ultrasound is one of the most widely used clinical modalities.

A major goal in small animal imaging is high throughput. The recent emergence of a small-animal high-frequency ultrasound imaging system has seen significant attention and been used by researchers in various fields, and has generated a large number of studies. While

primarily providing realtime anatomical imaging capabilities, color Doppler mode also enables functional visualization of blood flow, and increasingly quantitative estimates of blood velocities. Microbubbles [3] and perfluorocarbon nanodroplets [4] are being pursued as molecular imaging ultrasound contrast agents, offering potentially very high sensitivity.

Recently, high-frequency ultrasound has seen a successful union with optical imaging techniques in the form of photoacoustic imaging [5]. In photoacoustic imaging, nanosecond laser pulses incident on tissue generate acoustic signals due to thermal- and stress-confined thermoelastic expansion in subcutaneous absorbing structures such as microvessels. Photoacoustic signals are detected and reconstructed to form images of optical absorption. Since whole blood is over two orders of magnitude more absorbing than surrounding tissue for much of the visible spectrum, very high image contrast is attained. Because spatial resolution in photoacoustic imaging is determined by ultrasonic rather than optical parameters, multiply scattered light is tolerated. This is noteworthy since imaging depth beyond a transport mean-free path is possible, unlike approaches relying on minimally scattered photons, such as traditional optical microscopy methods and optical coherence tomography.

While diffuse-optical tomographic methods permit and rely on multiply-scattered light, their reconstruction methods are ill-posed, transport-regime reconstruction is challenging [6, 7], and fine spatial resolution is practically difficult to obtain due to factors such as regularization. Analogous to computed tomography, circular-scanning photoacoustic tomography (PAT) has been used for non-invasively visualizing small animal brains [8], including application to functional brain imaging [9]. More recently, Maslov et al [10] and Zhang et al [11] have demonstrated exquisite images of subcutaneous microvasculature using dark-field confocal photoacoustic microscopy (PAM), a raster-scanning-based reflection geometry imaging system. Unique to photoacoustic methods is the ability to image blood oxygen saturation as well as concentration of total hemoglobin [11-13]. Emerging photoacoustic methods are enabling molecular imaging in small animals, including imaging of gene expression [14] and cell receptors [15]. Unfortunately, long scan times are presently required in both scanning PAT and PAM.

Our goal was to construct a realtime high-frequency photoacoustic imaging system. In principle, using an ultrasound array transducer, a photoacoustic image can be formed from each laser shot by reconstructing photoacoustic signals received in parallel through array elements . The system described in this article approaches this goal but rather uses a small number of laser shots at a high-repetition rate to acquire signals in multiplexed mode. Even with the present multiplexing scheme, our system offers realtime performance.

While Niederhauser et al [16] used an array system to demonstrate photoacoustic imaging their system lacked realtime imaging capabilities, primarily due to the 10-Hz repetition rate of their laser system. Moreover, they used only 16 receive elements to form an image using a diagnostic frequency ultrasound array. Others [17-20] have also demonstrated the use of arrays for photoacoustic imaging, however for low diagnostic frequencies. Optical detection of ultrasound using Fabry-Perot etalons has led to emerging 2-D arrays, recently producing 3-D microvascular images in animals and human subjects [21]. While this technique offers considerable promise, the signal-to-noise ratio strongly depends on the laser power of a laser probe beam, and presently this often means the necessity of scanning the probe beam, necessitating many pulsed laser excitations, and sacrificing realtime performance. A high-frequency array system for photoacoustic microscopy was previously reported by our group [22], but realtime acquisition and display was lacking. To our knowledge, this is the first published report of a realtime high-frequency photoacoustic imaging system. We will demonstrate the realtime imaging capabilities of our system, quantify its performance, and present *in vivo* data.

2. Methods

Our system consists of a laser diode-stack pumped Nd:YLF Q-switched laser, a tunable dye laser, a high-frequency ultrasound array transducer, custom receive and control electronics, an

8-channel PCI digitizer, a multi-core PC, and an LCD monitor for realtime display. A diagram of the main components of the system is shown in Fig. 1. We will describe each main component below.
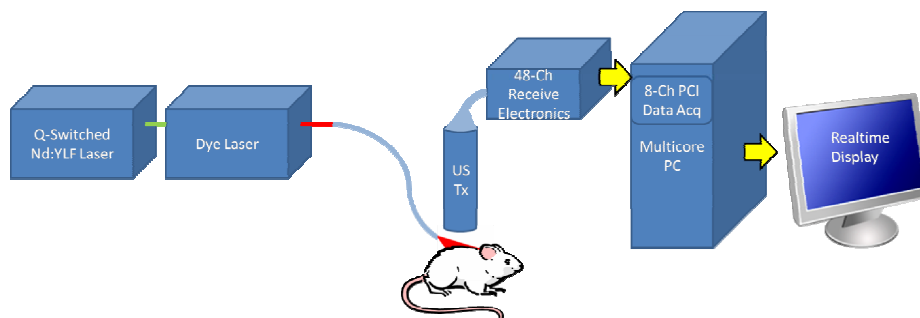

Fig. 1. Diagram of the key components of our realtime photoacoustic imaging system, including a KHz-repetition rate Q-switched pump laser, a dye laser, a fiber optic cable, an ultrasound transducer (US TX), receive electronics, a dual-socket quad-core CPU personal computer (PC) with an 8-Ch 125 MS/s data acquisition card, and a monitor for realtime display.

2.1 Optics

A Nd:YLF diode-pumped Q-switched laser (INNOSLAB, Edgewave GmbH, Germany) was used to produce 6-ns optical pulses of ~12 mJ at a wavelength of 524 nm. Optical pumping by continuous-wave laser diode stacks in our Nd:YLF laser provides the flexibility of external triggering on demand at rates up to 1 KHz, without pulse energy loss. For our imaging system, this feature is a significant advantage over flashlamp-pumped Q-switched lasers that typically must be maintained at a fixed pulse repetition rate, and typically support much lower pulse rates. This laser was used to pump a dye laser (Cobra, Sirah Laser –und Plasmatechnik GmbH, Germany) outfitted with a high flow-rate dye circulator to minimize photo-depletion of the dye at high-repetition rates. The tunable output of the dye laser (with Rhodamine 6G laser dye) enabled peak output power at 578 nm with a roughly 40-nm tuning range. At the isosbestic 570.2-nm wavelength (where oxy- and deoxy-hemoglobin have equal molar extinction coefficients), the 1/e attenuation length of light in whole blood is roughly 40 μm, hence a photoacoustic signal from a blood vessel should possess a bandwidth of roughly 37 MHz, which closely matches our 30-MHz ultrasound transducer's center frequency. The 2-3 mJ of dye laser output were coupled into a 600-μm optical fiber and light from the other end of the fiber was delivered obliquely past the ultrasound transducer array forming an oblong pattern on the skin along the array axis. The estimated fluence was 5-10 mJ/cm^2 per pulse, below the ANSI recommended Maximum Permissible Exposure of 20 mJ/cm^2. For our imaging experiments we used 578-nm and 571-nm wavelengths corresponding to the peak dye laser power and an isosbestic point, respectively.

2.2 High-frequency ultrasound array transducer

While diagnostic medical ultrasound systems typically operate in the 1-15 MHz range, the development of array systems with higher operating frequencies is more challenging and still in the research phase. Difficulties include fabricating arrays with small kerfs, interconnect issues, weak capacitive impedance of small elements, crosstalk, noise, and lack of adequate receive electronics. While higher frequencies promise finer imaging resolution, attenuation limits penetration.

To receive photoacoustic signals, we used a unique 30-MHz linear array transducer fabricated from a 2-2-piezo-composite by the NIH Transducer Resource Center at the University of Southern California [23]. The advantage of the piezocomposite material used in

our application is that it offers high piezo-electric properties (important for transducing weak photoacoustic signals) while the acoustic impedance of the material is greatly improved compared to pure piezoceramics [23].

Our array possessed 48 elements with 100-μm pitch (corresponding to 2λ where λ is the wavelength corresponding to the transducer center frequency), 19.1 dB compensated pulse-echo insertion loss, and element cross-talk below 25 dB. A fixed 8.2 mm elevation focus was provided, elements possessing 2-mm height. While the mean pulse-echo fractional bandwidth was 50%, this figure was improved to ~70% for receive only, used for our present photoacoustic imaging system.

2.3 Data acquisition and control electronics

Photoacoustic signals converted to voltage signals by the ultrasound array were amplified and conditioned prior to digitization. The 48 receive channels of the system were each amplified by pre-amplifiers (MAX4107, Maxim/Dallas Semiconductor), down-multiplexed 3:1 using RF multiplexer ICs (AD8184, Analog Devices), bandpass filtered with a 4th-order Butterworth filter, then amplified using a 40 dB variable gain amplifier (AD8332, Analog Devices). RF transformers (T1 6T, Minicircuits) are used to convert the differential output of the VGAs to a single line and a final 23 dB fixed gain stage offers a total variable gain between 33 and 73 dB. All these steps were implemented on an RF printed circuit board having 48 SMA inputs and 16 SMA outputs, described by Bitton et al [24]. The remaining 16 channels were down-multiplexed to 8 channels using modified MAX4141 multiplexer evaluation boards (Maxim, Inc). The final 8 lines were digitized at 125 MSPS using a 14-bit 8-channel PCI data acquisition card (Octopus CompuScope 8389, GaGe Applied Systems, USA) with 50 Ω input impedance. SMA-terminated RG-174 coaxial cables connected the array to the RF receiver board, the receiver board to the additional multiplexers, and the multiplexers to the data acquisition card. The PCI digitizer board was controlled using custom software written in C and C#, modified from the manufacturer's software development kits. The card had 128 MB of on-board memory, and the PCI bus offered 32-bit transfers at 66 MHz clock rates, providing data transfer to the PC RAM at better than 200 MBPS. Benchmark software written in C showed the system capable of sustained data acquisition and transfer to PC RAM for 1 KS records at roughly 1 KHz. The card was used as the master clock for our entire system, and was programmed to send out trigger signals to the multiplexer control and laser. In this way each laser trigger was guaranteed to be synchronized with the data acquisition clock, avoiding pulse-to-pulse jitter detrimental to multiplexed beamforming. For each B-frame to be acquired, the Gage card was programmed to record a sequence of 6 acquisitions, enabling multiplexed access to 48 array elements with 8 receive channels. Each acquisition was preceded by a trigger out signal with a specified delay time before recording. The repetition rate of the 6 acquisitions per B-frame, and accompanying trigger signals was set at 1-KHz, determined by the Gage card hardware, with the precision of the onboard 125MS/s clock. The inter-frame delay, however, was software controlled, and hence variable due to lack of interrupt control in the Windows operating system. Our hypothesis was that since a B-frame was acquired in only 6 ms, beamforming degradation due to motion over multiplexed data acquisition should be minimal. This hypothesis is addressed in the Results section.

The multiplexer control circuit consisted of a simple 4-bit counter, counting from binary 0 to 5. The counter was implemented using CMOS pre-settable counter integrated circuits (CD74HCT163E, Texas Instruments). At the beginning of the data acquisition cycle, parallel-port signals were used to toggle counter resets and count enables. Two bits of the counter output were used to control the 3 multiplexed states of the RF board, and a third bit was used to control the 2:1 MUX boards, as illustrated in Fig. 2. Trigger signals from the Gage card acted as the clock-input to the counter circuit, advancing the count, and changing the multiplexer state. A bit from the parallel-port was used to enable this trigger signal to pass to the laser via a D-latch. Since the Gage card's trigger out duration was too brief to reliably trigger the laser, a pulse-delay generator (DG535, Stanford Research Systems) was used to forward the trigger to the counter circuit with an expanded pulse width.
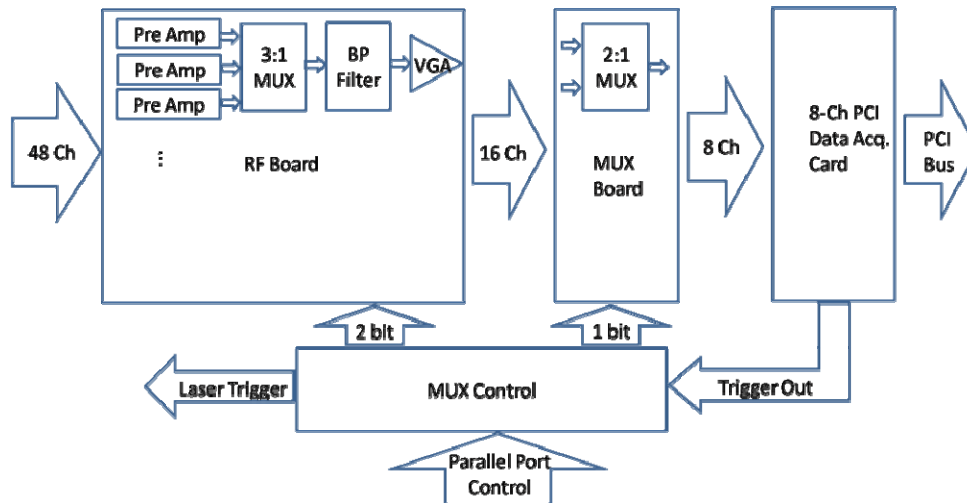
Fig. 2. Architecture of the receive and control electronics of our realtime photoacoustic imaging system. The 48 receive channels are boosted by pre-amplifiers, down-multiplexed (MUX), bandpass (BP) filtered, and amplified with a variable gain amplifier stage (VGA). The resulting 16 channels are down-multiplexed to 8 channels for digitization. Control electronics toggle through multiplexer states, and pass trigger signals to the laser.

2.4 Multi-Threaded Multi-Core Processor Approach to Parallel Beamforming

While ultrasound beamforming traditionally uses hardware such as application-specific integrated circuits (ASICs), or programmable hardware such as Field Programmable Gate Arrays (FPGAs) [25, 26], we instead explore multi-core processors for this task. This approach will allow off-the-shelf PCs to perform tasks that previously required dedicated hardware. Following Moore's 1965 projection that transistor densities will double every 18-24 months [27], and noting the recent trend in multi-core processors, we project that the software approach to beamforming may prove fruitful. Advantages include short high-level software development time, great flexibility for channel-domain processing and post-beamforming signal and image processing, and ease of upgrading to new processor powers.

Dynamic receive beamforming was implemented in C++ and compiled to a Dynamic Link Library in Visual Studio 2005 Professional Edition (Microsoft Corp.). Multi-threaded parallel programming was accomplished by using OpenMP pragmas before 'for' loops for each A-scan reconstruction, along with the appropriate variable scope declarations. OpenMP is a collection of instructions simplifying the shared-memory multi-threading and parallel programming process. Our beamforming algorithm leverages the computing power of our multi-core processors by parallel computation of A-scans of different scan angles. Delay values for the dynamic receive beamforming algorithm were computed once prior to all beamforming computations, and stored in memory similar as an effective look-up table. Since our sampling rate is close to the Nyquist limit which is sparse for delay and sum beamforming operations, channel data was up-sampled 5 times using simple linear interpolation prior to beamforming. During beamforming, channel-data was delayed by pre-computed values, using nearest neighbor interpolation. Delays were computed as

$$\tau_n(R,t) = \frac{x_n \sin\theta}{c} + \frac{x_n^2 \cos^2\theta}{2Rc} \tag{1}$$

where x_n is the distance to the array element from the center of the array, c is the speed of sound, and θ is the desired steering angle. As noted in Zemp et al [22], the first term of Eq. 1 represents steering and is identical to the pulse-echo ultrasound counterpart while the second determines focusing and differs from the pulse-echo ultrasound counterpart by a factor of two,

reflecting one-way, rather than two-way propagation. In this article, no coherence factor weighting was used as was applied previously. All 48 receive channels were used for each A-line in the beamformed image.

All operations were performed with pointers, abating the need for duplicate copies of data in the memory, and accelerating performance. Built-in compiler options were selected to optimize for speed. Benchmark tests beamforming 48 channels of 500 samples per channel into an image with 128 scan lines 500 samples deep were clocked at better than 83 frames per second on a fast PC (Dell Precision 490) with two 2.66 GHz Quad-core Xeon processors (with 8 MB of L2 cache and 1333 MHz front-side bus). The system possessed 4 GB of DDR2 SDRAM with a 667 MHz bus clock. This shared memory 8-core processor system represented one of the market's highest computing-power desktop PCs available at the time of this work (spring 2007). While the Xeon processors support 64-bit operations, the Gage card drivers were only available for 32-bit Windows and thus the available addressable RAM was limited to ~3 GB rather than the available 4 GB. It may be possible to significantly improve the 83 fps benchmark speed by further optimizing the beamforming algorithms using processor-specific assembly-language.

2.5 GPU-based scan conversion and display

Scan conversion refers to the process of mapping a matrix of beamformed data onto an appropriate curvilinear geometry. Scan conversion is often done with dedicated hardware, but may also be done with software. Since we wanted to reserve computing power for beamforming throughput, similar to [25], we decided to implement scan conversion and display using the Graphical Processing Unit (GPU) of the graphics card (128 MB PCIe x16 nVidia Quadro NVS 285) rather than the multi-core Central Processing Unit (CPU). Besides offloading computational burden from the CPU, GPU-based scan conversion allowed us to take advantage of a wide range of software tools for rendering graphics.

We used a novel approach to our scan conversion algorithm. Instead of computing each pixel of the curvilinear image by interpolation via a point-by-point coordinate transformation as is typically done, we rather instructed the graphics card to warp our pre-scan-converted image matrix onto a 32×32 or 64×64 mesh of triangles defining the curvilinear coordinates, shown in Fig. 3. This mesh was generated and stored in the graphics card memory prior to data streaming. The B-scan-images following beamformation were then written to the GPU in RGB-format and were then stretched onto the triangle mesh and displayed in the correct curvilinear format upon rendering. A new texture (pre-scan-converted B-mode image) was written to the GPU for each new frame. Zoom and pan capabilities were simply accomplished by keyboard-control of a virtual camera position above the scan-conversion mesh. Additionally, this approach provided vector-based rather than pixel-based rendering, offering smoothed rather than pixilated-looking images.

To implement these procedures, we used Microsoft XNA Game Studio in the Visual Studio C# Express Edition (Microsoft Corp.) environment. XNA is a new wrapper around the native Managed DirectX. Due to a well developed library, and graphic card-independent programming capabilities, this environment allowed rapid development of the rendering methods needed for realtime display. There are also some disadvantages. The use of pointers in C# is allowed but un-natural due to C#'s managed dynamic memory allocation and 'garbage' collector. Thus all CPU operations requiring speed were developed using C/C++ and these functions were compiled to Dynamic Link Libraries (DLLs), which were then called in the C# environment in the context of a so-called 'unsafe' scope.
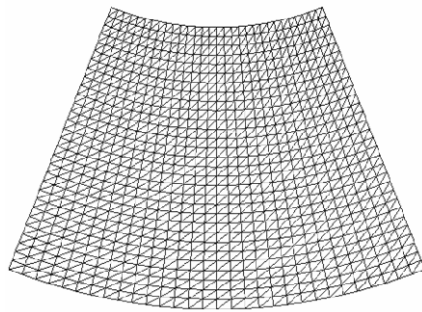
Fig. 3. To offload computational burden from the CPUs to the GPU, we implemented a 32x32 scan-conversion mesh over which the pre-scan converted beamformed image was warped using graphic-card rendering methods primarily developed for the video game industry.
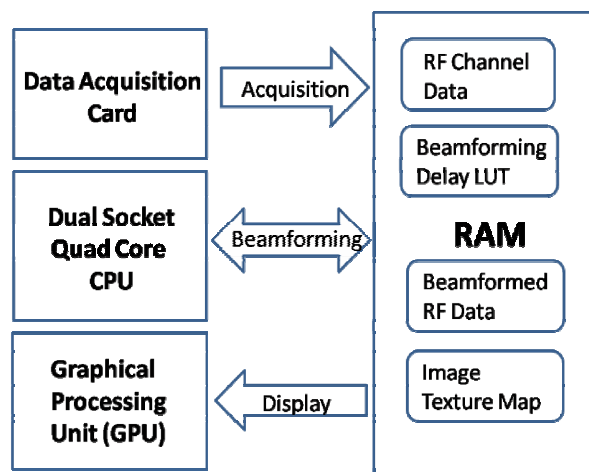

Fig. 4. Schematic of software communication between the data acquisition card, CPUs, GPU, and system RAM. Note that the acquisition, beamforming, and display operations were implemented on parallel threads. Since these operations read and write common resources, signaling flags were used to avoid access conflicts.

2.6 Parallel Threading Issues

Multiple parallel threads are instantiated in our software: one for data acquisition and transfer, another for beamforming, another for scan conversion and display, and another for a graphical user interface enabling data logging and display options. Daughter threads are also spawned from the beamforming thread via OpenMP to enable parallel reconstruction of A-scan lines as described above. If one process encounters an execution bottleneck, the other threads will continue to operate using the data available in the current state. Figure 4 shows how our software is organized to communicate between the PCI card, the CPUs, the GPU and the RAM. Note that some processes spawned on parallel threads require access to common data. Access to thread-sensitive resources is mediated by event-handling flags which are set and reset after each process completes its intended job. In this way potential conflicts between multiple threads are avoided.

2.7 Data archival and post-processing

Pre-beamformed channel data was archived to hard-disk for offline processing. A library of utility programs written in C++ and C# were used to perform rapid beamforming on archived data, and the post-beamformed RF data was written to file for envelope detection, scan conversion, and post-processing in MATLAB (Mathworks Inc). Post-processing operations included intensity transformations such as contrast stretching, and median filtering for edge-preserving noise reduction.

3. Results

3.1 Resolution study

To evaluate the system resolution, we constructed a phantom consisting of two crossed 6-μm-diameter carbon fibers suspended in water. Using a translation stage to move the probe relative to the phantom, we acquired images at progressive scan positions along the array's elevation direction. The maximum intensity C-scan projection image of the phantom is shown in Fig. 5(a). A representative B-scan near the dashed line location is shown in Fig. 5(b), and the maximum cross-range photoacoustic amplitude of this B-scan is shown in Fig. 5(c). These images demonstrate clearly distinguishable points separated at only ~80 μm (40 μm lateral separation and 70 μm vertical separation). At 6.9 mm imaging depth (normal depth from the transducer surface), the lateral resolution should be the product of the *f*# (6.9 mm / 4.8 mm = 1.44) times the center wavelength (50 μm), equal to 72 μm. The axial resolution measured in Zemp et al [22] was close to $\lambda/2$ at 25-30μm. Thus the clear 80 μm separation of carbon fibers is reasonable.
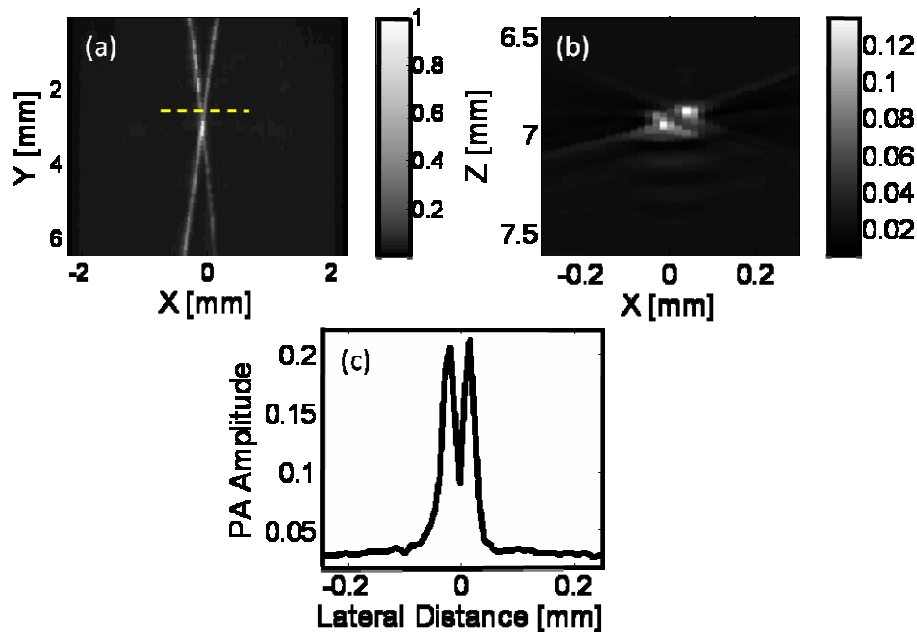

Fig. 5. (a) C-scan maximum amplitude projection image of crossed 6-μm carbon fibers, constructed from 50 parallel B-scans. (b) a sample B-scan at the dotted-line position in (a). The carbon fibers are separated here by only ~80 μm, yet are clearly distinguishable. (c) a cross-range maximum amplitude projection of (b) onto the x-axis.

3.2 Frame rate

Our software enabled the following three modes of operation: (1) high-speed acquisition but with no realtime display (2) realtime acquisition and display, and (3) realtime acquisition and display with continuous hard-disk data logging. In high-speed acquisition mode (1), the frame rate could be as high as 167 frames per second (1000 Hz divided by 6 laser shots per image). In this mode, the number of frames that could be acquired was limited by the memory depth of the data acquisition card. This mode may be valuable for studying small animals or embryos with very high heart rates. At 1000-Hz sustained repetition rate laser safety may be a concern as will be discussed. In mode (2), realtime acquisition and display, average frame rate was ~50 frames per second (fps). In mode (3) with continuous hard-disk data logging, frame-rate reduced to ~21 fps for ASCII file archival, but remained ~50 fps for binary formats. These results were obtained using an 80 GB SATA hard drive with an 8 MB cache and up to 3 GB/s transfer speed at 7200 rotations per minute. To verify the frame rate and to assess the inter-frame delays, an image frame trigger was recorded on an external oscilloscope (TDS5034, Tektronix). The frame trigger was obtained by taking the laser trigger signal and using a pulse-delay generator (DG535, Stanford Research Systems, Sunnyvale, CA) to produce a 7-ms-duration TTL pulse. Since each frame acquisition required a burst of 6 TTL laser triggers at 1-kHz repetition rate, with 7-ms hold-off time, the pulse-delay generator produced one image trigger per laser-trigger burst.

3.3 Evaluation of handheld performance

Because our data acquisition is multiplexed, we must realize that motion may not be tolerated if it is very fast. In particular, if we want the delay-and-sum beamforming computations to maintain coherence, inter-acquisition motion should be minimal, otherwise artifacts may be produced. By requiring that motion over our 6-ms acquisition time is less than $\sim\lambda/4$, we restrict ourselves to motions with velocities of less than ~2 mm/s. While this velocity is small, we can also realize that our field of view with appreciable signal-to-noise is only ~4 mm by 4 mm. Hence this velocity represents translation across half the field of view in 1 second.

To test the performance of the system against motion for handheld operation, we imaged a 100-μm human hair while translating the array. We performed this translation using hand motion but restricting motion to vertical and horizontal translations by means of an optical post-based translation guide. Movies of acquired photoacoustic images of the hair phantom demonstrating ~3 mm/s horizontal and vertical motions are shown in Fig. 6 and Fig. 7, respectively. No apparent distortion of the hair point-spread function was apparent. Note that images of the hairs appear to have a top and bottom lobe. This can be explained by noting that the top and bottom of the hair can be resolved with this system since the axial spatial resolution is ~25 μm.
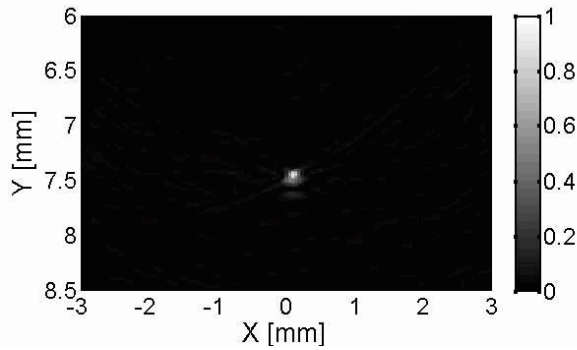
Fig. 6. Movie (2.5 MB) of photoacoustic B-scans of a human hair in water. The probe was moved up and down in an oscillating fashion using manual adjustment of a micrometer on a translation stage. This video sequence demonstrates the realtime capability of the system, specifically it's robustness to vertical motions.
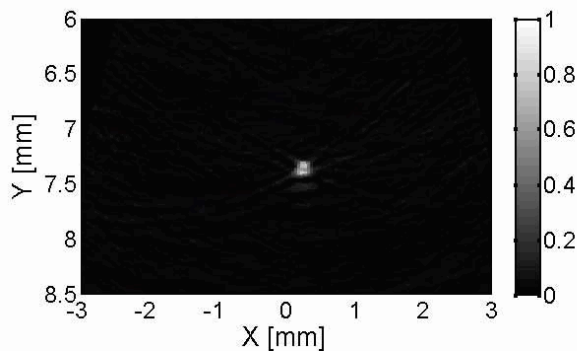

Fig. 7. Movie (3 MB) of photoacoustic B-scans of a human hair in water. The probe was moved laterally by hand along a guide rail. This video sequence demonstrates the robustness of the multiplexed acquisition scheme against horizontal motions.

3.4 In Vivo Depth Performance

To test *in vivo* performance, we imaged the upper thoracic region of young athymic nude mice (~10g, Charles River). In doing so we fixed the transducer using a custom holder, and placed it in a de-ionized water bath, beneath which we placed a nude mouse. Consumer-grade plastic wrap coated the container holding the water, and a window at the bottom allowed the water-filled membrane to contact the surface of the animal. Acoustic coupling gel or simply a thin layer of water was used to improve the acoustic coupling between the animal and the water-filled membrane. During imaging the nude mouse was anesthetized using a gas anesthesia machine (EZ-5000, Euthanex Corp., Palmer, PA) with 1-2% vaporized isofluorane at an air flow-rate of 1-1.5 L/min. Absorbing structures were detected above the noise floor to depths of 2.5-3 mm in vivo, as shown in Fig. 8.
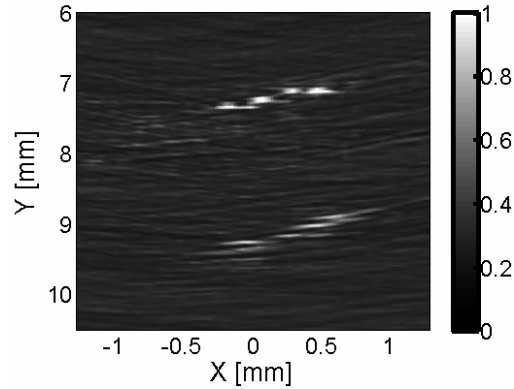
Fig. 8. Photoacoustic image of microvasculature in a nude mouse. This figure demonstrates appreciable signal to depths of ~2.5 mm.

3.5 In Vivo Static and Dynamic Imaging

The multimedia file of Fig. 9 shows a movie of microvascular structures, where the subject and transducer are fixed relative to each other. Electronic noise generates a visible flicker in the images, but because the system is realtime, the eye tends to provide a good temporal filter to distinguish static structures from random noise. The movie linked to Fig. 10 shows a 2-way fly-through of microvessels, where the array is translated over 10-15 mm along the array's elevation direction forwards then backwards. Notice the prominent oblique vessel structure which seems to be moving across the bottom of the field of view.
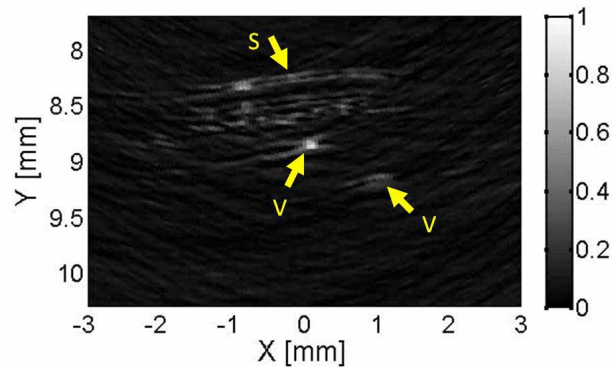

Fig. 9. (3.2 MB) Photoacoustic movie sequence of subcutaneous microvasculature as the subject and probe are held in a fixed position. S is the skin surface and bright regions below the skin surface are microvessels including venules and arterioles. Two sample vessels are labeled with the letter V in the figure.
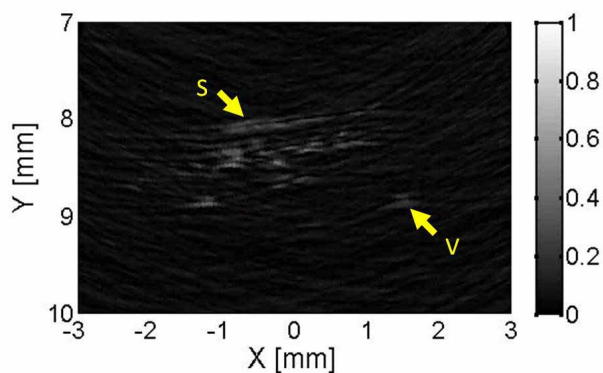
Fig. 10. (4MB) Photoacoustic movie sequence of a 2-way fly-through across 10-15 mm over the skin surface S. Notice the prominent oblique vessel V move from the middle right to the center of the image and back as the array is translated along its elevation direction.

4. Discussion

The system presented here represents the first realtime high-frequency photoacoustic imaging system to our knowledge, and we have seen a glimpse of its capabilities. There is considerable room for forward progress and we now offer a discussion of such avenues.

Thus far, we have performed only single wavelength imaging. Future work may incorporate multiple-wavelength illumination for spectral estimation of blood oxygen saturation and other physiological parameters of interest. A fast-tuning laser source would be highly desirable for this application.

Presently the light delivery approach is not amenable to direct probe-skin contact and the transducer must be held above the skin surface. Future improvements should integrate a standoff mechanism to better control light delivery and facilitate contact measurements as this adds to handheld stability. It is important to consider the laser exposure of tissue with our technique. The laser energy induced temperature rise is given by the heating equation, $\Delta T = Q / \rho V C_P$, where Q is the energy delivered, ρ is the density, V the volume of the heated region, C_p the specific heat of blood (4.18 J/g/°C) and ΔT the temperature rise. With 10 mJ/cm^2 of 578-nm laser fluence Φ, the temperature rise in the $d=2/e=68$-μm absorption layer in a blood vessel is given as $\Delta T = \Phi A / \rho d A C_P = \Phi \rho d C_P \approx 0.35^0 C$ per laser pulse, which is independent of the vessel size. While for pulsed lasers emitting visible light, the ANSI recommended fluence is only 20 mJ/cm^2, some applications use much more. For US Food and Drug Administration (FDA)-approved applications such as tattoo removal and laser-induced bleaching of port-wine stains it is more typical to use fluences on the order of 6 J/cm^2 using 585-nm light (over 600 times the ANSI recommendation) without known permanent damage. In such applications, the expected temperature rise in vessels below the skin surface is in excess of 60°C [28].

The thermal relaxation time, defined as the time at which the mean blood vessel temperature drops to half the initial value immediately after laser pulse heating, is given as $\tau_r = d_{BV}^2 / 16\chi$ [29] where d_{BV} is the blood vessel diameter (or the absorption-region, whichever is smaller), and χ is the thermal diffusivity of skin, typically 0.11 mm^2/s [29]. For vessels with diameters of 10, 70 and 150 μm, τ_r has calculated values of 0.06, 2.8 and 12.8 ms, respectively. For a 80-μm absorption layer (~2/e at 578 nm) the thermal relaxation time is ~3 ms. For a frame rate of 50 fps the inter-frame delay is 20 ms, and we expect heat to have dissipated to 0.01 of its peak value by the time another frame-burst is initiated.

For exposure times longer than 10 s, the ANSI recommended limit for skin illumination is 200 mW/cm^2, a number designed to limit cumulative laser-induced heating. For <10 s dwell

times, the maximum permissible exposure is limited by $1100t_e^{1/4}$ in mJ /cm^2, where t_e denotes the exposure duration in seconds. For our case, since we send a rapid train of 6 pulses followed by an inter-frame delay which is long enough for heat to adequately dissipate (as note above for 50 fps rates), we take the exposure duration as 6 ms. This corresponds to a total of 54.4 mJ/cm^2 delivered over the 6 pulses, translating into ~9 mJ/cm^2 per pulse, which is roughly our present fluence, even though our average power delivery is ~3 W/cm^2, above the CW ANSI limit. Higher imaging frame rates may induce undesirable laser-heating.

Heating can be minimized in future systems incorporating more digitization channels since the requirement for multiplexing is reduced. More acquisition channels will also reduce possible motion artifacts for very fast motions, and allow for increased energy fluence per laser pulse, which will improve the signal-to-noise ratio and penetration depth. For significant penetration depths, a broader surface illumination may be advantageous as this will enable more multiply-scattered photons to be delivered to a given depth.

A broader illumination pattern will also increase our field of view. Presently our field of view with any appreciable signal-to-noise ratio is limited to ~3-4 mm axially and laterally. This is largely due to light delivery and penetration. Note however, that since our array transducer possesses 2λ pitch, grating lobes may be problematic for large steering angles. Thus, to increase the field of view we should also use a transducer with smaller pitch (although such transducers are presently difficult to fabricate), and more elements.

Future system designs should also take great care to design the RF electronics to reduce noise as much as possible – to approach the theoretical best-case Johnson (thermal) noise floor.

Finally, it is presently difficult to interpret our B-scan images without some reference image of the anatomical context. For this reason it would be greatly advantageous to integrate high-frequency pulse-echo ultrasound imaging capabilities in the system.

5. Conclusions

We have presented a first-of-its kind realtime high-frequency photoacoustic imaging system, have outlined our design including the hardware and software architecture, and have shown phantom and *in vivo* data. The B-scan acquisition rate is 50 frames/s, faster than the 30-Hz video rate. Also noteworthy is that this is the first article to our knowledge documenting realtime beamforming on a multi-core CPU desktop PC with high-level software, although others have certainly moved towards programmable hardware at a lower-level [30]. Because of the recent trend to multi-core processors, and leveraging Moore's Law, we may expect that our multi-threaded software approach may have considerable potential for photoacoustic systems, ultrasound systems, and other multi-channel systems requiring beamforming as the number of processor cores expands. Having provided some discussion on the capabilities and limitations of our realtime photoacoustic imaging system, one question that remains to be seen is what biomedical applications can best make use of this emerging technology. With recent progress, realtime photoacoustic imaging is sure to find a niche in several biomedical applications. Now equipped with realtime imaging capabilities, photoacoustic imaging is ready to make seminal contributions in biological and clinical imaging.